Supplementary Material

1 Supplementary Tables

Supplementary Table S1 | Ascending (ASC) and descending (DSC) interferometric pairs. The corresponding parameters are used for filtering with the adaptive phase filter (see text).

Track	Pair	Perpendicular baseline	Filter exponent	Filter Window size [pixel]	Step size [pixel]
DSC	20170819-20170910	5.8	0.35	64	8
DSC	20171126-20171207	54.7	0.35	64	8
DSC	20171207-20171218	58.9	0.8	128	16
DSC	20171218-20180109	-289.5	0.8	128	16
ASC	20170721-20170812	157.9	0.35	64	8
ASC	20171119-20171130	-85.8	0.5	256	32
ASC	20171130-20171211	49.6	0.8	256	32
ASC	20171211-20180102	117.2	0.5	256	32

2 Supplementary Figures

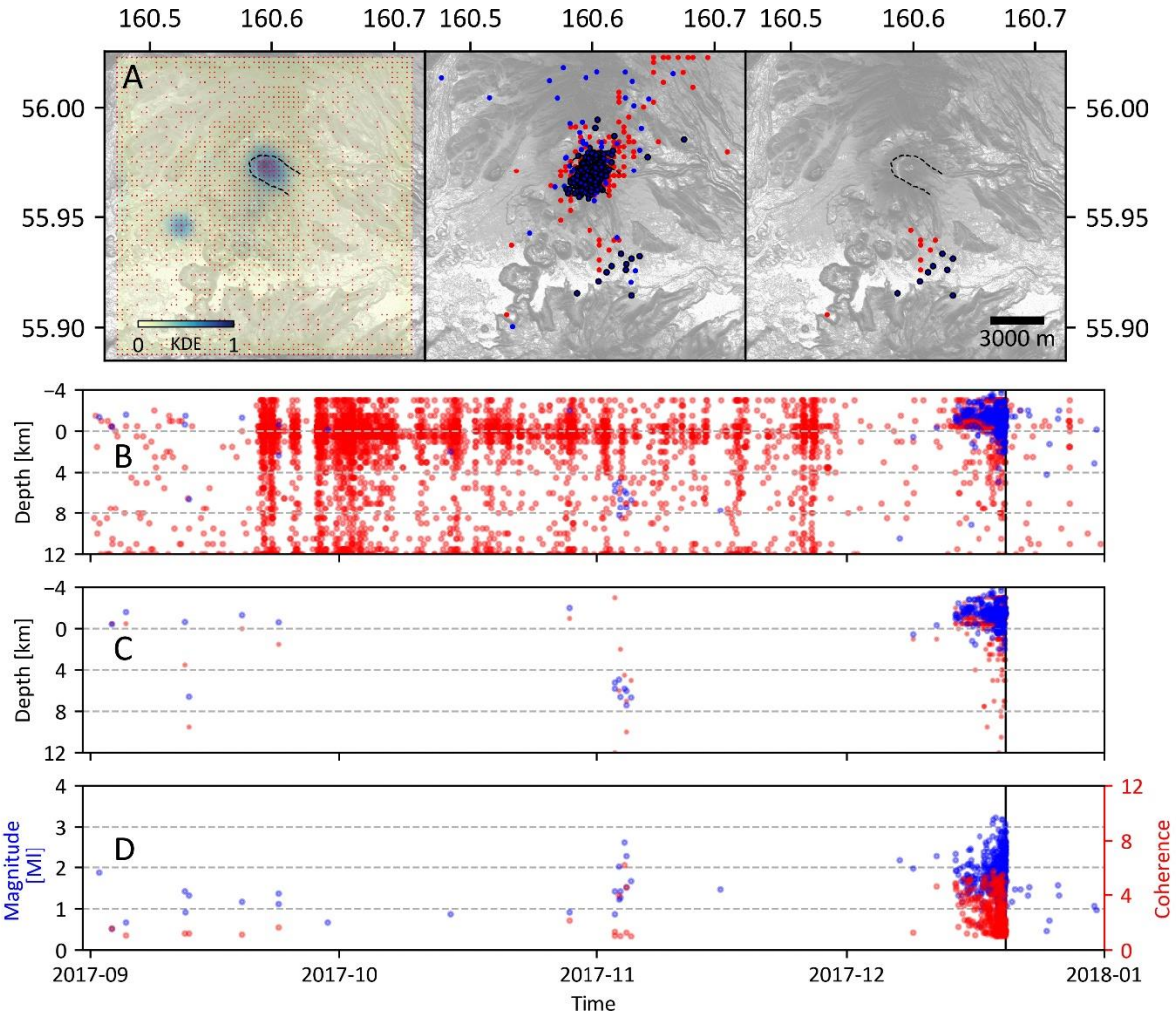

Supplementary Figure S1 | Comparison between events detected by the Lassie algorithm (Lassie events) and events detected by Koulakov et al. **(**2021**;** reference events). (**A**, left panel) Kernel density estimation (KDE) used as a heatmap to highlight were most of the Lassie events (red dots) are distributed in the lateral domain. (**A**, middle panel) Reference events (black) that were detected within 5 seconds from the corresponding Lassie events (red). Blue points show the remaining reference events. (**A**, right panel) Reference events (black) and Lassie events (red) that are detected within 5 seconds from the Lassie events (red) during 2–6 November 2017. (B) The depth distribution for all Lassie events (red) and all reference events (blue). (C) The depth distribution for events

detected with a time window of 5 seconds. (D) The corresponding coherence of the Lassie events and the local Magnitude (Ml) of the reference events.

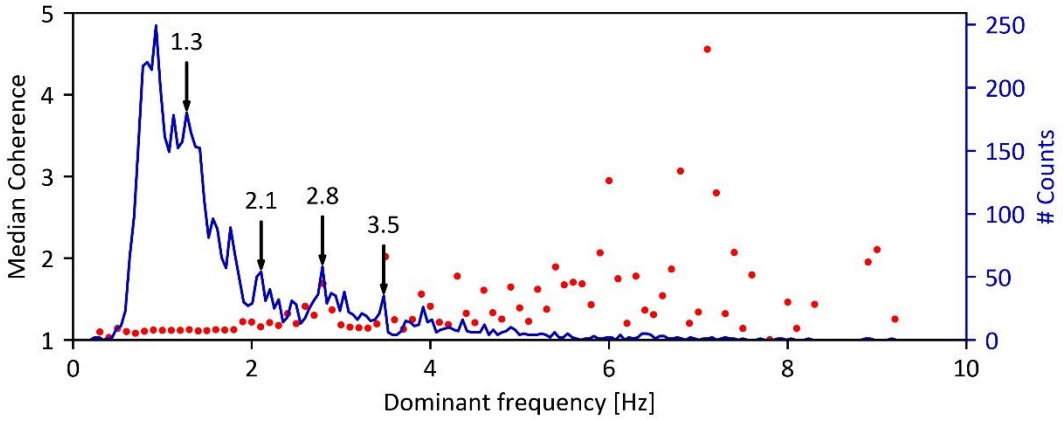

Supplementary Figure S2 | Distribution of the frequency of events (red dots) detected by the Lassie algorithm and the corresponding smoothed probability density function (blue line). Indicated peaks and numbers refer to frequency families used for further analysis (cf. Supplementary Figure 3).

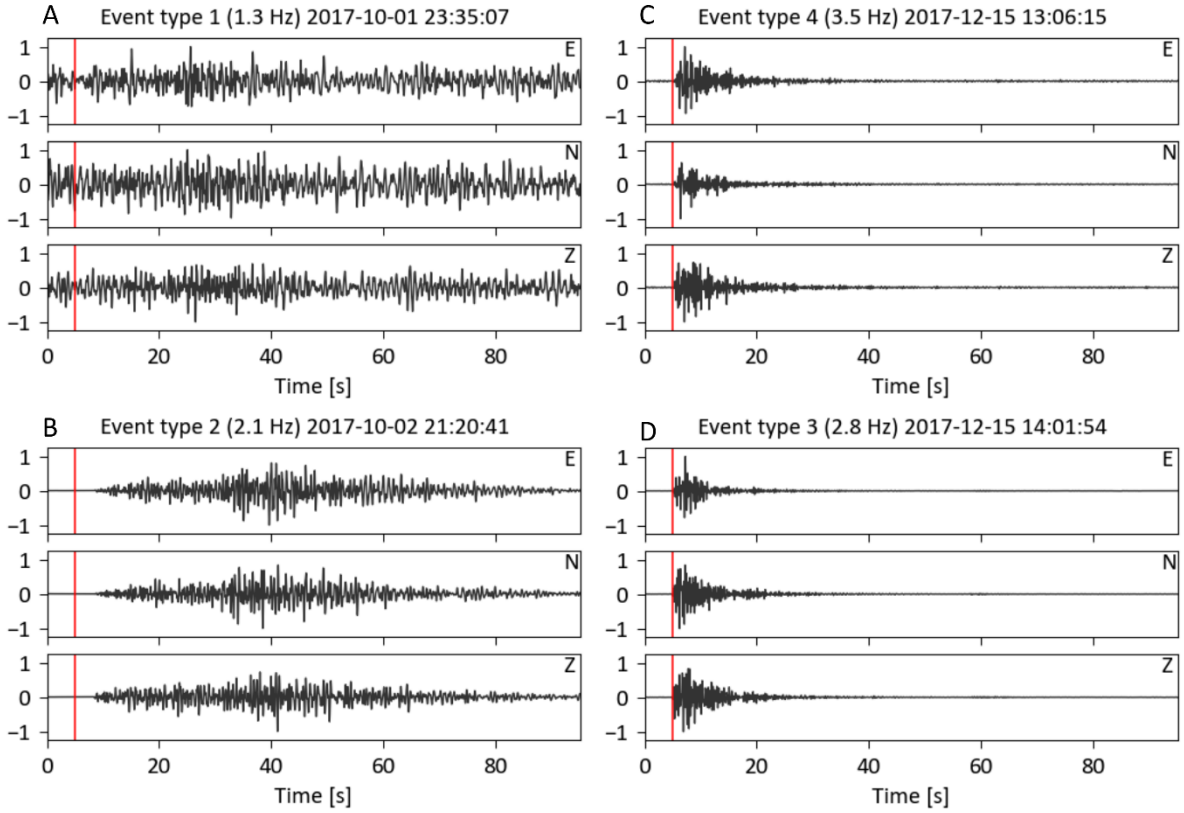

Supplementary Figure S2 | The four different selected event types detected by Lassie (cf. Supplementary Figure 2). **(A,B)** Low frequency event types that are referred to as long period (LP) events in the main text. **(C,D)** Higher frequency event types that are referred to as volcano-tectonic

(VT) events in the main text. The waveforms are band-pass filtered between 1-4 Hz. The detection times are indicated by the red vertical lines.

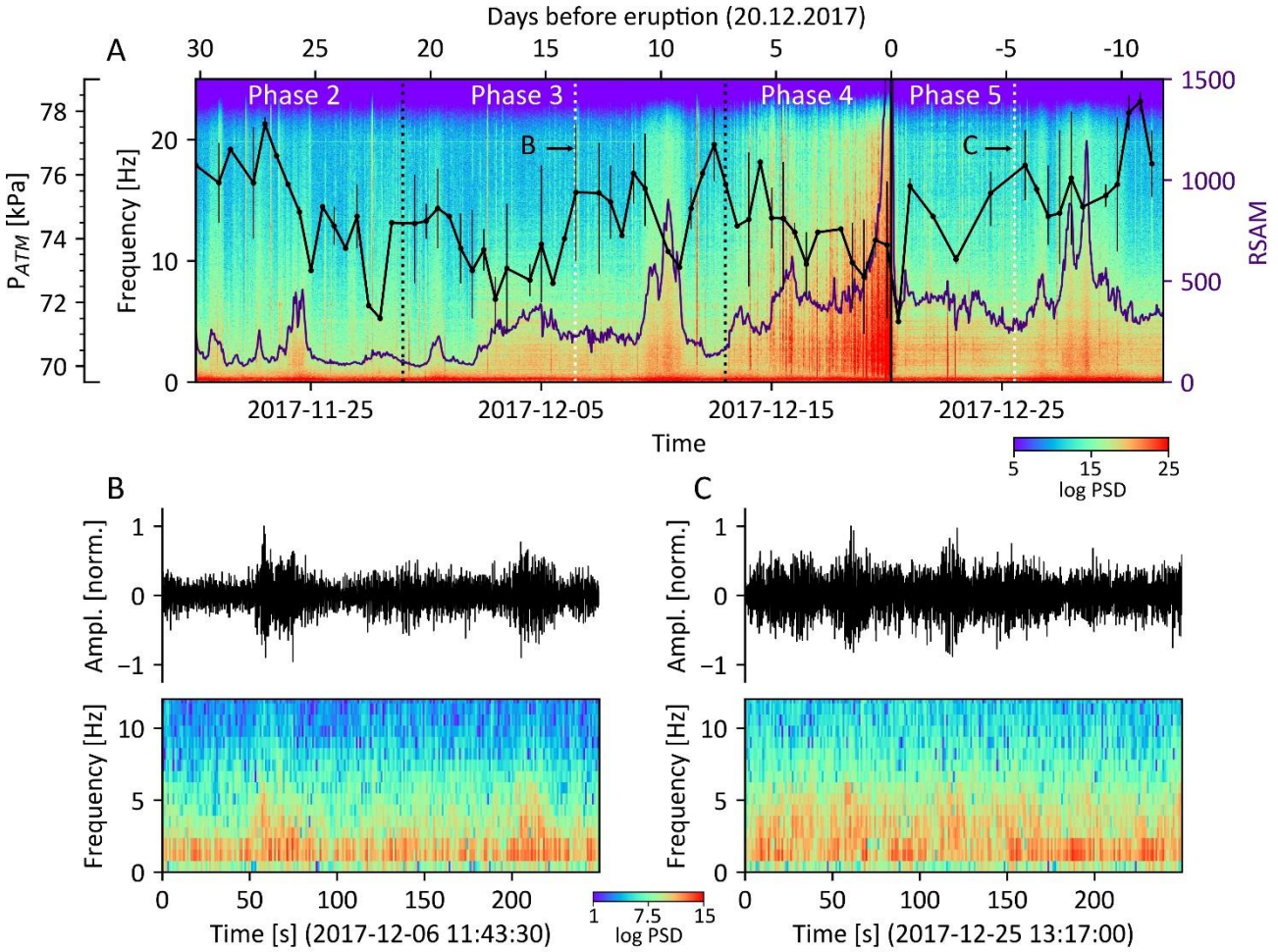

Supplementary Figure S4 | Seismic and meteorological results between 20 November and 31 December 2017. **(A)** Real-time seismic amplitude measurements (RSAM, purple line) of station B01 (vertical component) and spectrogram in background. The power spectral density (PSD) of the spectrogram details the amount of seismic amplitude present in the seismic signal as a function of the seismic frequency. 12-hourly atmospheric pressure (P_{ATM}, black line) measured at altitudes between 2–2.5 km over the town of Klyuchi. Dots indicate the mean and the error bars the corresponding measured extremes. Black dotted lines indicate the separation between the volcanic phases (cf. Figure 2). White dashed lines show the timing for example waveforms and corresponding spectrograms of station B01 (vertical component) depicted in **(B,C)**.

Supplementary Figure S5 | Time-lapse camera images showing the changing intensity of degassing at Bezymianny starting shortly after the 16 June 2017 eruption until 3 January 2018. Indicated times

are in UTC and numbers in brackets refer to days before the eruption. P1-P5 correspond to the phases indicated in Figure 2. The camera was located close to seismic station B04 (cf. Figure 1B).

Supplement Figure S6 | Time-lapse camera images showing partial snow coverage on Bezymianny's upper flanks where differential interferometry identified deformation (cf. Figure 4E,F,

Figure 6). The different phases correspond to the phases indicated in Figure 2. The camera was located close to seismic station B06 (cf. Figure 1B).

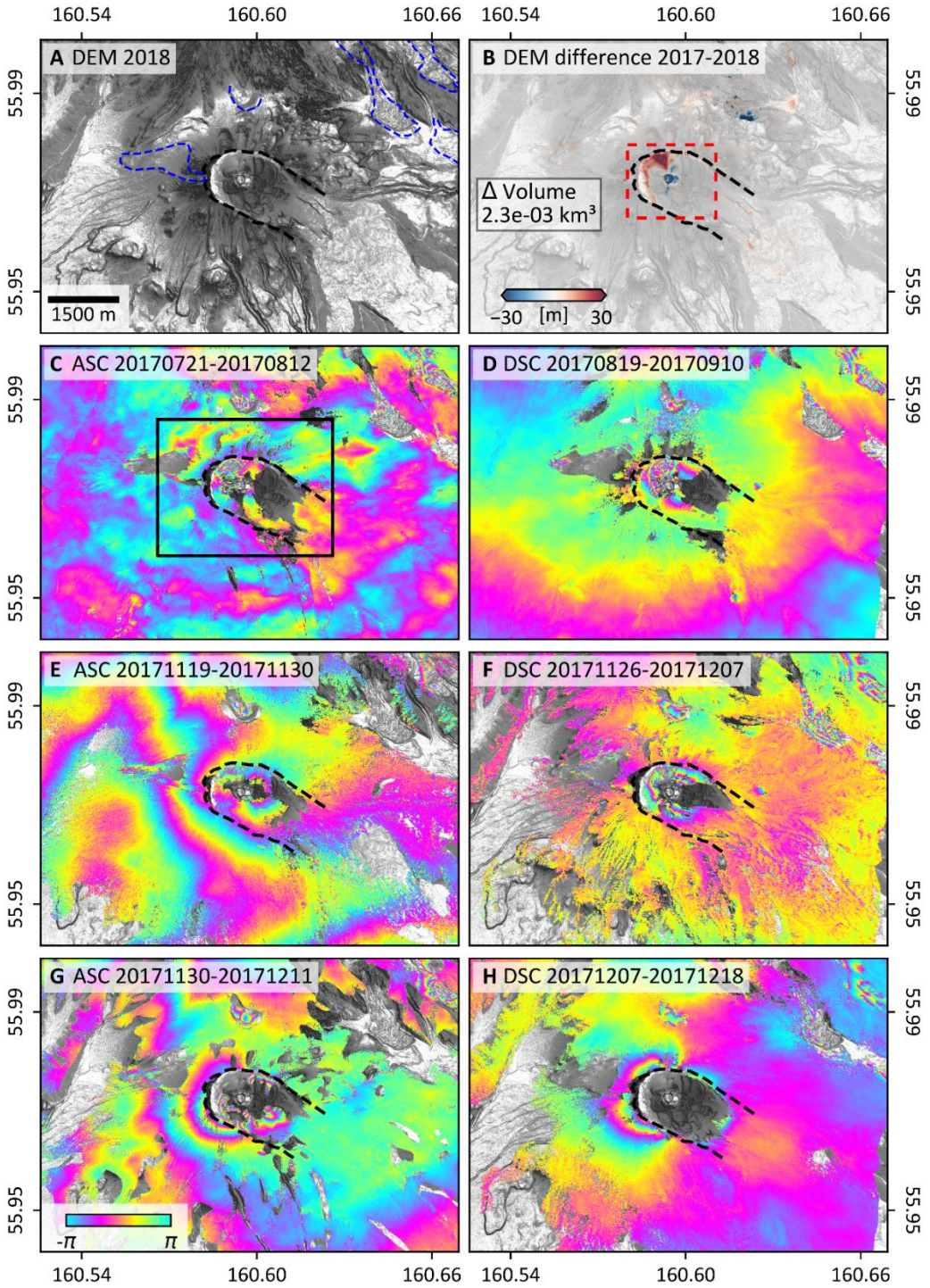

Supplementary Figure S7 | (A) Bidirectional hillshade of Bezymianny's topography after the 20 December 2017 eruption. The black dashed line delineates the 1956 collapse scar. Blue dashed lines indicate the locations of rock glaciers (RG). **(B)** Difference between the topography before and after the investigated eruption. The red dashed box shows the region used to calculate the erupted volume. The negative difference to the north of Bezymianny may be related to shadows in the optical data

used to generate the digital elevation model. **(C,D)** Ascending (ASC) and descending (DSC) interferograms showing displacements within the amphitheater after the 16 June 2017 eruption. **(E-H)** ASC and DSC interferograms showing the evolution of ground deformation before the 20 December 2017 eruption. Please note that most interferograms indicate that the rock glaciers in the vicinity of Bezymianny are constantly moving.

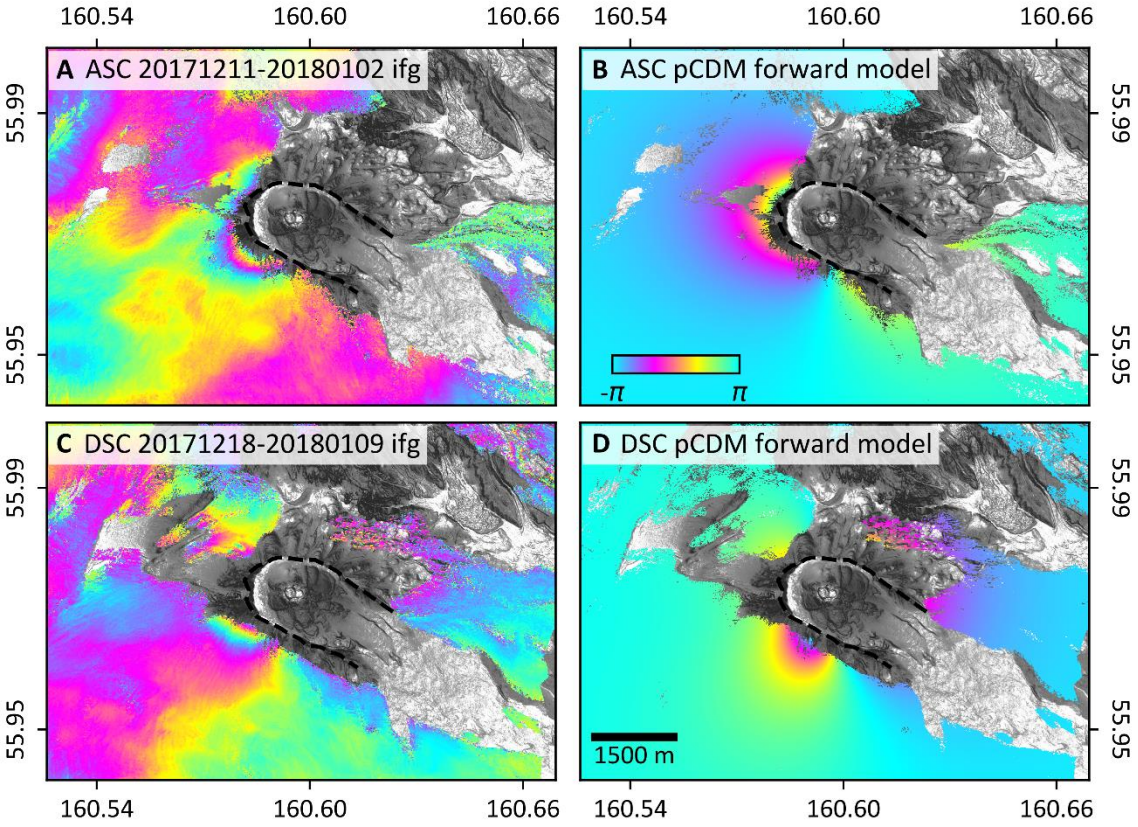

Supplementary Figure S8 | Raw interferograms **(A,C)** showing inverted surface deformation after the 20 December 2017 eruption (cf. Figure 3E,F). To infer the source of deformation, we computed

the corresponding forward models **(B,D)** by using the inverted volumes determined for the inversion of deformation before the eruption (cf. Figure 4, Table 2).

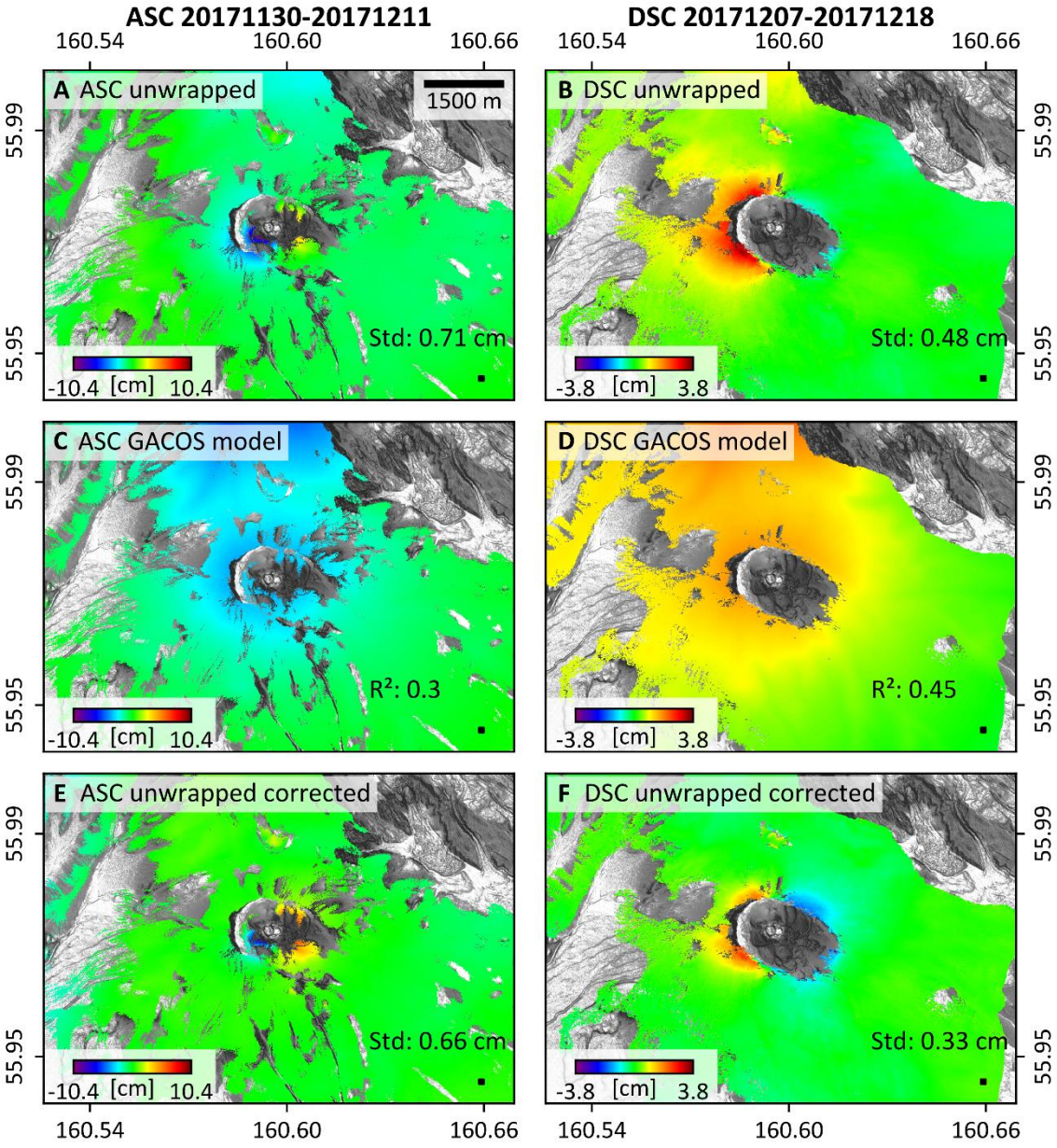

Supplementary Figure S9 | Atmospheric corrections of the unwrapped phase of the ascending (ASC) and descending (DSC) tracks **(A,B)** using the corresponding GACOS weather models **(C,D)**. **(E,F)** Corrected interferograms. The black square denotes the reference window where deformation is considered to be zero.

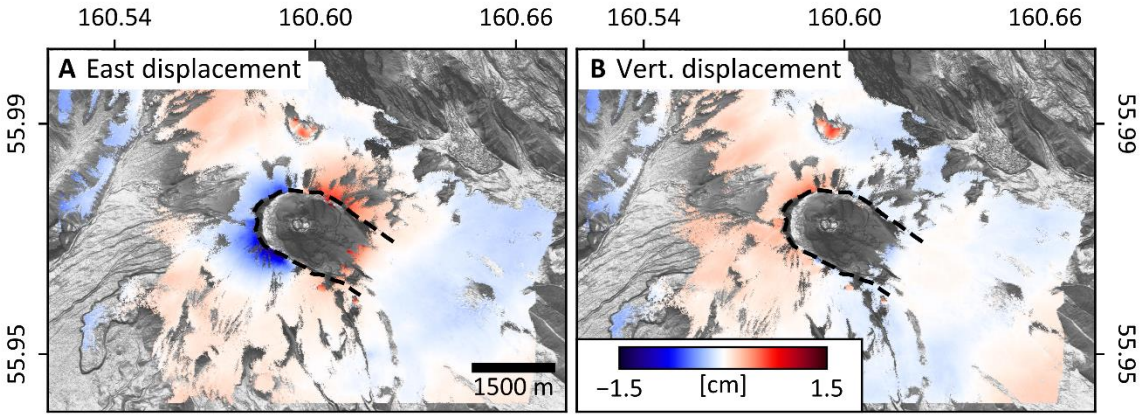

Supplementary Figure S10 | Decomposition of the pre-eruptive ascending (20171130-20171211) and descending (20171207-20171218) interferograms based on the approach from Wright et al. (2004). **(A)** and **(B)** depict the corresponding east and vertical components.

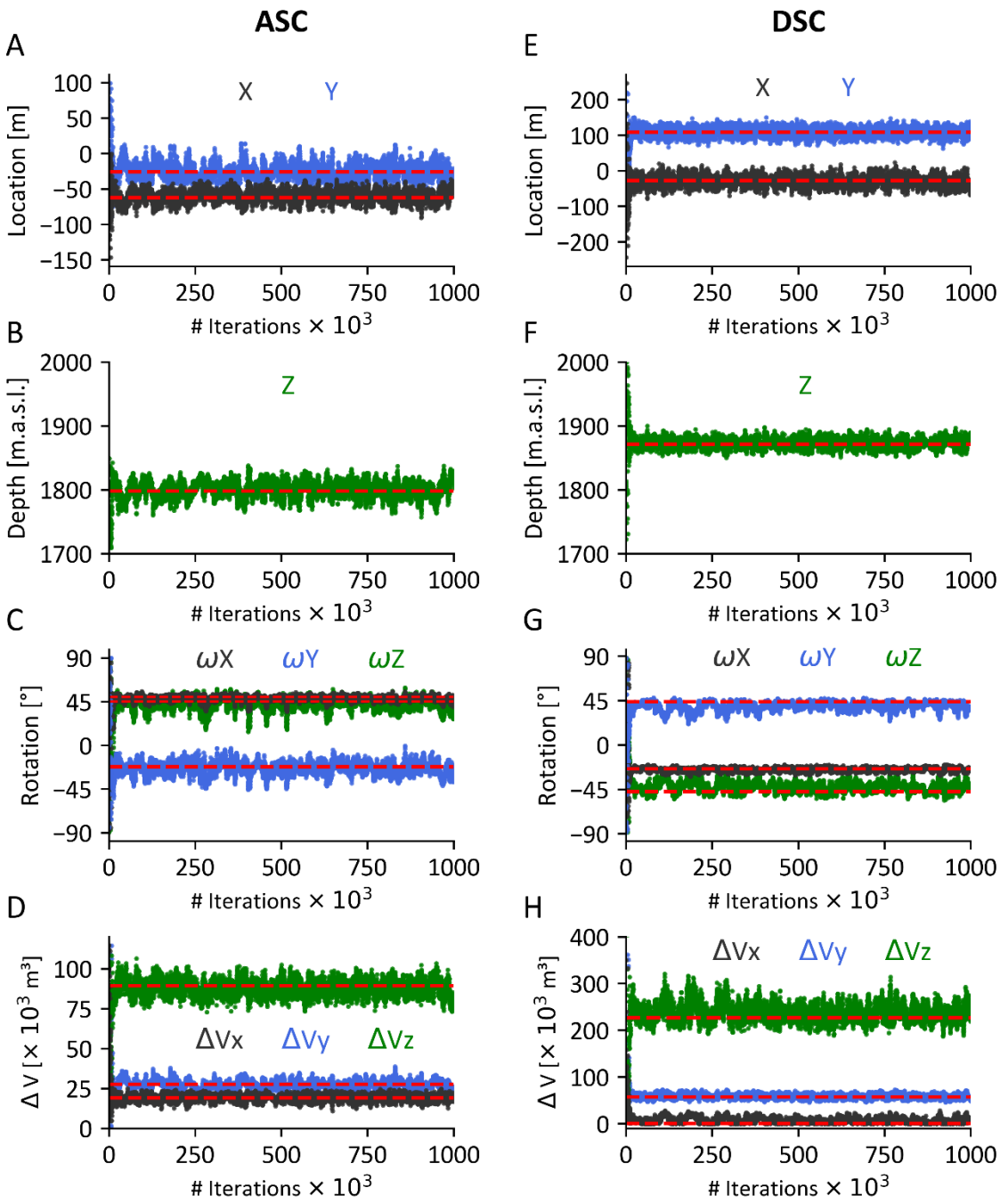

Supplementary Figure S11 | Illustration showing the convergence of the pCDM parameters during the source inversion with GBIS software (Bagnardi & Hooper, 2018). **(A,E)** Lateral location parameters X and Y, **(B,F)** depth Z, **(C,G)** rotation angles round the three axis, and **(D,H)** volumetric

changes along the three axis of the pCDM. The red dashed lines indicate the corresponding optimal values.

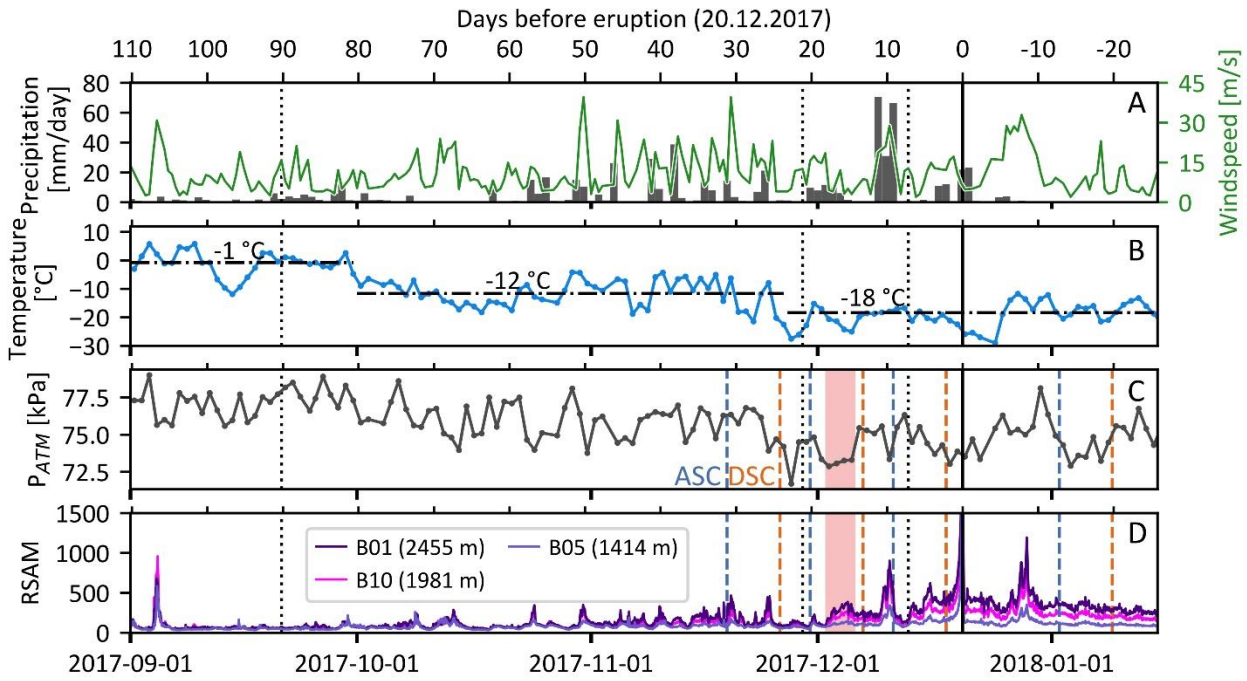

Supplementary Figure S12 | **(A)** Daily mean precipitation (dark gray bars) over Bezymianny volcano derived from TRMM/GPM data (Huffman et al., 2019) and the evolution of the 12-hourly-median wind speed (green line) measured at altitudes between 2 and 2.5 km over the town of Klyuchi (cf. Figure 1A). **(B)** Daily mean temperature measured at altitudes between 2–2.5 km. Horizontal dash-dotted lines indicate the average temperature for selected periods. **(C)** Daily mean atmospheric pressure (P_{ATM}) measured at altitudes between 2–2.5 km. Blue and orange vertical dashed lines refer to the acquisition time of the ascending (ASC) and descending (DSC) tracks, respectively. **(D)** Evolution of the absolute real-time seismic amplitude (RSAM) of the vertical component of selected stations. The red shaded area indicates a period of potential anti-correlation between P_{ATM} and RSAM.

3 References used for the Supplementary Material

Bagnardi, M., and Hooper, A. (2018). Inversion of Surface Deformation Data for Rapid Estimates of Source Parameters and Uncertainties: A Bayesian Approach. *Geochemistry, Geophys. Geosystems* 19, 2194–2211. doi:10.1029/2018GC007585.

Wright, T. J., Parsons, B. E., and Lu, Z. (2004). Toward mapping surface deformation in three dimensions using InSAR. *Geophys. Res. Lett.* 31, 1–5. doi:10.1029/2003GL018827.